Zentrum für Technomathematik
Fachbereich 3 – Mathematik und Informatik

Image Sequence Interpolation based on Optical Flow, Segmentation, and Optimal Control

Kanglin Chen **Dirk A. Lorenz**

Report 11–11

Berichte aus der Technomathematik

Report 11–11 **December 2011**

Image Sequence Interpolation based on Optical Flow, Segmentation, and Optimal Control

Kanglin Chen, and Dirk A. Lorenz

***Abstract*—When using motion fields to interpolate between two consecutive images in an image sequence, a major problem is to handle occlusions and disclusions properly. However, in most cases one of both images contains the information which is either discluded or occluded; if the first image contains the information (i.e. the region will be occluded), forward interpolation shall be employed, while for information which is contained in the second image (i.e. the region will be discluded), one should use backward interpolation. Hence, we propose to improve an existing approach for image sequence interpolation by incorporating an automatic segmentation in the process which decides in which region of the image forward resp. backward interpolation shall be used.**

Our approach is a combination of the optimal transport approach to image sequence interpolation and the segmentation by the Chan-Vese approach. We propose to solve the resulting optimality condition by a segregation loop, combined with a level set approach. We provide examples which illustrate the performance both by RMSE and human perception.

***Index Terms*—Active contours, image sequence interpolation, optimal control, optical flow, segmentation, transport equation.**

I. Introduction

IMAGE sequence interpolation is the generation of intermediate images between two given consecutive images, a process which is, for example, relevant if image acquisition is slow or expensive and has broad applications in the fields of video compression, medical imaging and so on. In video compression, the knowledge of motions helps to remove the non-moving parts of images and compress video sequences with high compression rates. For example in the MPEG format, motion estimation is the most computationally expensive portion of the video encoder and normally solved by mesh-based matching techniques [1]. While decompressing a video, intermediate images are generated by warping the image sequence with motion vectors. In the field of medical imaging image sequence interpolation is also desired. For example, the diagnostic requires a point by point correspondence between the same tissue from the image sequence taken at difference time [2]. Moreover, image sequence interpolation is also able to improve the quality of historic movies by increasing the frame-rate to the modern standard. Similarly, in disease diagnostics an image of a patient's tissue may need to compare with a healthy tissue [3]. This is an example of how image sequence interpolation in some cases can be used to solve the application normally classified as image registration. However, in this article we focus on movie-like image sequences; these sequences are notably different from registration problems in that we may have different objects which move in different directions resulting in disclusions and occlusions.

Considering the problem of image sequence interpolation, the optical flow (the measurable 2D motion field between two images) plays a decisive role. Since Horn and Schunck proposed the variational method to estimate optical flow in their celebrated work [4], this field has been widely developed. To preserve the flow edges non-linear isotropic constraint was applied instead of the linear constraint of the Horn & Schunck method [5], [6], an anisotropic diffusion constraint improved the preservation of edges by an oriented smoothness constraint in which smoothness is not imposed across edges [7], [8], and the TV-L^1 method is not only able to preserve the flow edges but also able to work robustly against the outliers [9].

There are several existing variational methods based on optical flow to interpolate missing intermediate images. In [10] the variational method penalized by the elastic regularization is considered:

$$J_{\mathrm{rigid}}(u,b) = \int\limits_{[0,T]\times\Omega} (u_t + b\cdot\nabla u)^2 + \lambda\left|\nabla b' + \nabla b\right|^2 dxdt,$$

where b denotes the optical flow and $\nabla b'$ denotes the transpose of the Jacobi matrix of b. Hence, they do not exactly enforce the brightness constancy constraint $u_t + b\cdot\nabla u = 0$ but penalize its violation as in the classical Horn & Schunck approach. Minimizing this functional gives the interpolated images with maximal rigidity, and has applications in the field of medical image registration, e.g. registration of magnetic resonance images. In [11] the authors keep the assumption of brightness constancy without differentiating it and update the flow field with the help of robust estimators. There the authors also incorporated object based motion segmentation. In [12] the authors also keep the assumption of brightness constancy without differentiating it and apply the time dependent Horn & Schunck functional:

$$J_{\mathrm{cons}}(b) = \frac{\lambda}{2}\int_0^T \|u(t) - u_T\|^2_{L^2(\Omega)}\,dt + \frac{1}{2}\int_0^T\int_\Omega |\nabla b|^2\,dxdt,$$

where $u(0) = u_0$ and u_T are the given two images. After calculating the time-dependent optical flow one can warp the initial image u_0 to a certain time. In [13] the authors do enforce the brightness constancy constraint again and minimize a functional with the equation $u_t + b\cdot\nabla u = 0$ as a constraint.

Different from the global variational methods are the so-called pixel-wise methods. In [14] the path-based interpolation sequence method is considered. There one searches where every pixel comes from and traces out the path of every pixel from the given two images. To stabilize the interpolation and to handle occlusion, a post-processing is used by means of verification of the displacement flow. In [15], [16] another pixel-wise method is introduced, namely the perception-based interpolation. They simulate human visual perception in the following way: To begin with, they detect the edges and homogeneous regions, and then they estimate the translets by matching edges; finally they use the forward warping and feather the interpolated images.

Besides the above mentioned image sequence interpolation methods, the image warping technique was introduced in [17] to generate the intermediate image based on a priori known optical flow field, e.g. estimated by the Horn & Schunck method. However, this kind of optical flow may not be suitable for image sequence interpolation, see [12], [15]. In [18] we introduced a more natural way to utilize optical flow into image sequence interpolation under the framework of optimal control similar to [13]. This method can be applied to the cases that image sequence obeys rigid and non-rigid movements, and also works robustly against noise.

In this paper we aim to eliminate a common drawback of all flow-based methods for image image sequence interpolation: While using forward interpolation it is impossible to obtain good results for regions which are disclosed, since any method has to guess the appearing pixels. Similarly, backward interpolation will fail in regions which are occluded. To solve this problem we propose an extension of our method proposed in [18] which incorporates a segmentation process for the image domain to automatically detect regions in which forward resp. backward interpolation shall be employed.

The paper is organized as follows: In Section II we review the segmentation model by Chan and Vese [19] while in Section III we recall the basics of our proposed optimal control approach to image sequence interpolation. Section IV presents the combination of both approaches and Section V presents details on the numerics.

II. Segmentation with Active Contours

The classical active contours models or snakes [20], [21] are widely used in image segmentation. However, in these models an edge detector related to the image gradient is required to stop the evolving curve on the boundaries of objects. In [19] Chan and Vese introduced a model based on active contours and the Mumford-Shah segmentation [22], which does not require an edge detector. Consequently, this model can detect contours both with or without gradient, for example for the objects with very smooth boundaries or even with discontinuous boundaries. We review the model of active contours without edges for the sake of completeness.

Let us define a curve C as the boundary of an open subset ω of a bounded domain $\Omega \subset \mathbb{R}^2$. Assume that C segments Ω into ω and $\Omega \setminus \overline{\omega}$, and the constants c_1, c_2 depending on C, are the average of the image u inside of C and respectively outside of C. Denoting with $|C|$ the length of C and with $|\omega|$ the area of ω, the segmentation will be achieved by minimizing the following energy

$$F(c_1,c_2,C) = \lambda_1 \int\limits_{\omega} |u-c_1|^2\,dx + \lambda_2 \int\limits_{\Omega\setminus\overline{\omega}} |u-c_2|^2\,dx + \mu|C| + \nu|\omega|, \tag{1}$$

where $\mu \geq 0, \nu \geq 0, \lambda_1, \lambda_2 > 0$ are the regularization parameters. To minimize (1) one uses a level set formulation. Suppose C is represented by the zero level set of a Lipschitz function $\phi : \Omega \to \mathbb{R}$, such that

$$\begin{cases} C = \partial\omega = \{x \in \Omega : \phi(x) = 0\}\,, \\ \omega = \{x \in \Omega : \phi(x) > 0\}\,, \\ \Omega \setminus \overline{\omega} = \{x \in \Omega : \phi(x) < 0\}\,. \end{cases}$$

Using the Heaviside function H and one-dimensional Dirac measure δ_0 defined as

$$H(z) = \begin{cases} 1 & \text{if } z \geq 0, \\ 0 & \text{if } z < 0, \end{cases}, \quad \delta_0(z) = \frac{d}{dz}H(z),$$

one can reformulate (1) in the following way:

$$\begin{aligned} F(c_1,c_2,\phi) = \lambda_1 &\int\limits_{\Omega} |u-c_1|^2\, H(\phi(x))\,dx \\ &+ \lambda_2 \int\limits_{\Omega} |u-c_2|^2\,(1 - H(\phi(x)))\,dx \\ &+ \mu \int\limits_{\Omega} \delta_0(\phi(x))\,|\nabla\phi(x)|\,dx \\ &+ \nu \int\limits_{\Omega} H(\phi(x))\,dx. \end{aligned}$$

In order to compute the associated Euler-Lagrange equations with respect to ϕ, one chooses a smooth approximation H_s and $\delta_s = H_s'$, e.g.

$$\begin{aligned} H_s(z) &= \frac{1}{2}\left(1 + \frac{2}{\pi}\arctan\left(\frac{z}{s}\right)\right), \\ \delta_s(z) &= \frac{1}{s\pi}\cos^2\left(\arctan\left(\frac{z}{s}\right)\right), \end{aligned}$$

which converge to H (pointwise a.e.) and δ (in the sense of distributions) as $s \to 0$. Let us define for $s, \varepsilon > 0$ the functional $F_{s,\varepsilon}$ by

$$\begin{aligned} F_{s,\varepsilon}(c_1,c_2,\phi) = \lambda_1 &\int\limits_{\Omega} |u-c_1|^2\, H_s(\phi(x))\,dx \\ &+ \lambda_2 \int\limits_{\Omega} |u-c_2|^2\,(1 - H_s(\phi(x)))\,dx \\ &+ \mu \int\limits_{\Omega} \delta_s(\phi(x))\,|\nabla\phi(x)|_\varepsilon\,dx \\ &+ \nu \int\limits_{\Omega} H_s(\phi(x))\,dx, \end{aligned}$$

where $|\cdot|_\varepsilon$ denotes the ε-smoothed total variation functional defined by

$$|\nabla\phi|_\varepsilon = \sqrt{|\nabla\phi|^2 + \varepsilon}.$$

To minimize $F_{s,\varepsilon}$ with respect to ϕ, one deduces the associated Euler-Lagrange equations for ϕ and parameterizes the descent direction by an artificial time $t \geq 0$. The equation in $\phi(t,x)$ with the initial contour $\phi(0,x) = \phi_0(x)$ is

$$\begin{cases} \dfrac{\partial \phi}{\partial t} = \delta_s(\phi)\left(\mu \nabla \cdot \left(\dfrac{\nabla \phi}{|\nabla \phi|_\varepsilon}\right) - \nu - \lambda_1 (u - c_1)^2 \right. \\ \qquad \left. + \lambda_2 (u - c_2)^2 \right) \text{ in } (0,\infty) \times \Omega, \\ \phi(0) = \phi_0 \text{ in } \Omega, \\ \dfrac{\delta_s(\phi)}{|\nabla \phi|_\varepsilon} \dfrac{\partial \phi}{\partial n} = 0 \quad \text{on } \partial\Omega. \end{cases} \tag{2}$$

where $\partial\phi/\partial n$ denotes the normal derivative of ϕ on the boundary.

III. Optical Flow based Optimal Control for Image Sequence Interpolation

Given two consecutive images u_0 and u_T, we desire to find a flow field such that the field drives the transport equation with the initial value u_0 to fit u_T at time T as well as possible. This process has been accomplished in [18] under the framework of optimal control, and we briefly review this method: Consider the Cauchy problem for the transport equation in $[0,T] \times \Omega$, $\Omega \subset \mathbb{R}^2$:

$$\begin{cases} \partial_t u(t,x) + b(t,x) \cdot \nabla u(t,x) = 0 \quad \text{in }]0,T] \times \Omega, \\ u(0,x) = u_0(x) \quad \text{in } \Omega, \\ u_n(t,x) = 0 \quad \text{in }]0,T] \times \partial\Omega. \end{cases} \tag{3}$$

Here the (time dependent) flow field is denoted by $b : [0,T] \times \Omega \longrightarrow \mathbb{R}^2$, the image function depending on t and x is denoted by u and u_n denotes its normal derivative. The Neumann boundary condition $u_n = 0$ is not essential in this case, since we assume that b vanishes on $\partial\Omega$ for a.e. $t \in]0,T]$ in the following context.

Our intention is to find a flow field b such that the "transported" image $u(T)$ at time T matches the image u_T as well as possible. This motivates us to minimize the functional $\frac{1}{2}\|u(T) - u_T\|^2_{L^2(\Omega)}$. However, this problem is ill-posed, and hence we add an additional regularization term in the cost functional. In addition, we add the divergence-free constraint of b and obtain an optimal control problem as follows for a given $\lambda > 0$: Minimize

$$J(b) = \frac{1}{2}\|u(T) - u_T\|^2_{L^2(\Omega)} + \frac{\lambda}{2}\int_0^T \|\nabla b(t,\cdot)\|^2_{L^2(\Omega)^4}\, dt.$$

$$\text{subject to} \quad \text{div} b = 0 \text{ and (3).}$$

The associated Karush-Kuhn-Tucker system for the optimal control problem uses a dual variable p for the constraint (3) and a dual variable q for divergence-free constraint and is given by

$$\begin{cases} u_t + b \cdot \nabla u = 0 \text{ in }]0,T] \times \Omega, \text{ with } u(0) = u_0 \text{ in } \Omega, \\ p_t + b \cdot \nabla p = 0 \text{ in } [0,T[\times \Omega, \text{ with } p(T) = -(u(T) - u_T) \text{ in } \Omega, \\ \lambda \Delta b + \nabla q = p \nabla u \text{ in } [0,T] \times \Omega, \\ \text{div} b = 0 \text{ in } [0,T] \times \Omega, \qquad\qquad , \text{ with } b = 0 \text{ on } \partial\Omega. \end{cases} \tag{4}$$

According to the conservation law [23] and the divergence theorem [24], the divergence-free constraint of b makes the flow volume conserving, smooth and varying not too much inside of a moving object. At least the last two properties are desirable for computation of the optical flow. Moreover, the divergence-free constraint is a somehow technical assumption as it implies that the equation for the dual variable p of u is also a transport equation, and hence simplifies the numerical implementation.

To solve (4) numerically we apply a modified segregation loop. We suppose $n = 1, \cdots, N_{\text{loop}}$ and N_{loop} is the iteration number. Given u_0, u_T, $b^{n-1}(t)$, λ. The iteration process at iteration n proceeds as follows:

1) Compute $u^{n-1}(t), \nabla u^{n-1}(t)$ and $u^{n-1}(T)$ by the forward transport equation using u_0 and $b^{n-1}(t)$.
2) Compute $p^{n-1}(t)$ by the backward transport equation using $-(u^{n-1}(T) - u_T)$ and $b^{n-1}(t)$.
3) Compute the solution of the Stokes equations with right-hand side $p^{n-1}(t)\nabla u^{n-1}(t)$ and λ. Then, denote it by $\delta b^{n-1}(t)$.
4) Update $b^n(t) = b^{n-1}(t) + \delta b^{n-1}(t)$.

Although the segregation loop does not solve (4) directly, in [18] is shown that the modification with the update δb^{n-1} actually solves the necessary conditions of another optimization problem, namely: Minimize

$$\frac{1}{2}\|u(T) - u_T\|^2_{L^2(\Omega)}$$

subject to

$$\begin{cases} u_t + b \cdot \nabla u = 0 \text{ in }]0,T] \times \Omega, \text{ with } u(0) = u_0 \text{ in } \Omega, \\ \text{div} b = 0 \text{ in } [0,T] \times \Omega, \text{ with } b = 0 \text{ on } \partial\Omega. \end{cases}$$

From the point of view of regularization theory, one may see this segregation loop as a kind of a Landweber method for minimizing $\|u(T) - u_T\|^2_{L^2(\Omega)}$ which is inspired by a Tikhonov-functional.

IV. Optical Flow and Segmentation based Optimal Control for Image Sequence Interpolation

A. Modeling

Observing the movement of objects in an image sequence we may divide the domain into the "covered" domain and the "disclosed" domain. The "covered" domain refers to the regions in which the characteristics of two different pixels starting at time 0 end up at time T in a same place. Obviously, the "covered" domain is suitable for the forward interpolation from 0 to T. In the contrast, the "disclosed" domain refers to the regions in which no characteristic of a pixel starting at time 0 ends up at time T in a place. Since our interpolation method under the framework of optimal control will produce a continuous optical flow, in the “disclosed” domain will be filled-in with the neighbors, and hence we get a dense optical flow. But using the filled-in optical flow is still impossible to recover the objects in the “disclosed” domain, if we only take information from u_0. To overcome this drawback, which is inherent in all flow-based methods, we can apply a backward interpolation from T to 0 in the “disclosed” domain, i.e. the “disclosed” domain is turned to the “covered” domain in this case. An illustrative example of this phenomenon is the dataset MiniCooper[1] which is shown in Fig. 2. In the zoomed-in sub-images one easily observes that in the upper part of the head region and the rear part of the car, some new objects (pixels) appear.

Motivated by this explanation we propose to apply active contours to achieve an automatic selection process of the regions for forward or backward interpolation. To that end we incorporate the Chan-Vese segmentation process described in Section II into our optimal control framework from Section III. Moreover, we modify our optimal control framework in that we use a smoothed TV penalty for the flow field b to obtain sharper edges for flow. We assume that b vanishes on $\partial\Omega$ and model the evolving curve C in Ω as the boundary of an open subset ω of Ω. The forward interpolation, denoted by $\hat{u}$, shall take place in the set ω and backward interpolation $\tilde{u}$ shall be used in $\Omega \setminus \omega$. Hence, our cost functional is defined as

$$L(b,C,\omega) = \frac{1}{2}\left\|\hat{u}(T)-u_T\right\|^2_{L^2(\omega)} + \frac{1}{2}\left\|\tilde{u}(0)-u_0\right\|^2_{L^2(\Omega\setminus\overline{\omega})} + \lambda\int_0^T\int_\Omega \sqrt{\left|\nabla b\right|^2+\varepsilon}\,dxdt + \mu\left|C\right| + \nu\left|\omega\right|. \tag{5}$$

governed by the forward transport equation

$$\begin{cases} \hat{u}_t + b\cdot\nabla\hat{u} = 0 \ \text{ in }]0,T]\times\Omega, \\ \hat{u}(0) = u_0 \ \text{ in } \Omega, \end{cases}$$

the backward transport equation

$$\begin{cases} \tilde{u}_t + b\cdot\nabla\tilde{u} = 0 \ \text{ in } [0,T[\times\Omega, \\ \tilde{u}(T) = u_T \ \text{ in } \Omega, \end{cases}$$

and the divergence-free equation

$$\operatorname{div} b = 0 \ \text{ in } [0,T]\times\Omega.$$

The desired interpolation u at time t is estimated by

$$u(t,x) = \begin{cases} \hat{u}\left(t,x\right), & x\in\omega, \\ \tilde{u}\left(t,x\right), & x\in\Omega\setminus\overline{\omega}, \end{cases} \tag{6}$$

Actually, minimizing (5) we obtain the optical flow and the active contours for interpolation. Although we do not compute $u(t)$ directly from (5), in Section V we shall see that it is necessary to compute $\hat{u}(t)$ and $\tilde{u}(t)$ by computing the optical flow and active contours. Thus, interpolating $u(t)$ from (6) requires almost no additional computation.

[1] http://vision.middlebury.edu/flow/data/

To turn the cost functional (5) into a functional which is computationally feasible we follow the lines of Chan and Vese described in Section II: We assume that ϕ is the zero level set of C introduced in Section II and use a smoothed Heaviside function to reformulate (5) in terms of level set as

$$\begin{aligned} J_{s,\varepsilon}(b,\phi) = {} & \frac{1}{2}\int_\Omega \left|\hat{u}(T)-u_T\right|^2 H_s(\phi)\,dx \\ & + \frac{1}{2}\int_\Omega \left|\tilde{u}(0)-u_0\right|^2 \left(1-H_s(\phi)\right)dx \\ & + \lambda\int_0^T\int_\Omega \sqrt{\left|\nabla b\right|^2+\varepsilon}\,dxdt \\ & + \mu\int_\Omega \delta_s(\phi)\left|\nabla\phi\right|_\varepsilon dx + \nu\int_\Omega H_s(\phi)\,dx. \end{aligned} \tag{7}$$

B. First-order Necessary Optimality Conditions

We obtain the first-order necessary optimality conditions by defining the Lagrangian (with Lagrange multipliers $\hat{p}$, $\tilde{p}$ and q) as

$$\begin{aligned} & L(\hat{u},\tilde{u},b,\phi,\hat{p},\tilde{p},q) \\ & = \frac{1}{2}\int_\Omega \left|\hat{u}(T)-u_T\right|^2 H_s(\phi)\,dx \\ & + \frac{1}{2}\int_\Omega \left|\tilde{u}(0)-u_0\right|^2 \left(1-H_s(\phi)\right)dx \\ & + \lambda\int_0^T\int_\Omega \sqrt{\left|\nabla b\right|^2+\varepsilon}\,dxdt + \int_0^T\int_\Omega \left(\hat{u}_t + b\cdot\nabla\hat{u}\right)\hat{p}\,dxdt \\ & + \int_0^T\int_\Omega \left(\tilde{u}_t + b\cdot\nabla\tilde{u}\right)\tilde{p}\,dxdt + \int_0^T\int_\Omega q\operatorname{div} b\,dxdt \\ & + \mu\int_\Omega \delta_s(\phi)\left|\nabla\phi\right|_\varepsilon dx + \nu\int_\Omega H_s(\phi)\,dx. \end{aligned}$$

Finally, the necessary optimality conditions system consists of

1) The forward transport equation and its adjoint equation

$$\begin{cases} \hat{u}_t + b\cdot\nabla\hat{u} = 0 \ \text{ in }]0,T]\times\Omega, \\ \hat{u}(0) = u_0 \ \text{ in } \Omega, \\ \hat{p}_t + b\cdot\nabla\hat{p} = 0 \ \text{ in } [0,T[\times\Omega, \\ \hat{p}(T) = -\left(\hat{u}(T)-u_T\right)H_s(\phi) \ \text{ in } \Omega. \end{cases} \tag{8}$$

2) The backward transport equation and its adjoint equation

$$\begin{cases} \tilde{u}_t + b\cdot\nabla\tilde{u} = 0 \ \text{ in } [0,T[\times\Omega, \\ \tilde{u}(T) = u_T \ \text{ in } \Omega, \\ \tilde{p}_t + b\cdot\nabla\tilde{p} = 0 \ \text{ in }]0,T]\times\Omega, \\ \tilde{p}(0) = \left(\tilde{u}(0)-u_0\right)\left(1-H_s(\phi)\right) \ \text{ in } \Omega. \end{cases} \tag{9}$$

3) The TV$_\varepsilon$-Stokes equations (cf. [25])

$$\begin{cases} \lambda\nabla\cdot\left(\dfrac{\nabla b}{|\nabla b|_\varepsilon}\right)+\nabla q=\hat{p}\nabla\hat{u}+\tilde{p}\nabla\tilde{u} \ \text{ in } [0,T]\times\Omega, \\ \operatorname{div} b=0 \ \text{ in } [0,T]\times\Omega, \\ b=0 \ \text{ on } \partial\Omega. \end{cases} \tag{10}$$

4) The equation for segmentation

$$\begin{cases} \delta_s(\phi)\Big(\mu\nabla\cdot\left(\dfrac{\nabla\phi}{|\nabla\phi|_\varepsilon}\right)-\nu-\dfrac{1}{2}\left|\hat{u}(T)-u_T\right|^2 \\ \quad +\dfrac{1}{2}\left|\tilde{u}(0)-u_0\right|^2\Big)=0 \quad \text{in } \Omega, \\ \dfrac{\delta_s(\phi)}{|\nabla\phi|_\varepsilon}\dfrac{\partial\phi}{\partial n}=0 \quad \text{on } \partial\Omega. \end{cases} \tag{11}$$

V. Numerical aspects

To solve the forward and backward transport equations (8) and (9) we utilize the method of characteristics by solving the associated ODE using Runge-Kutta 4th order [26]. To solve the TV$_\varepsilon$-Stokes equations (10) at time t we apply the following iterative procedure to update b and q with time step Δt

$$\begin{aligned} b^{n+1}(t)&=b^n(t)+\Delta t\Bigg(\nabla\cdot\left(\frac{\nabla b^n(t)}{|\nabla b^n(t)|_\varepsilon}\right)+\frac{1}{\lambda}\nabla q^n(t) \\ &\qquad -\frac{1}{\lambda}\hat{p}(t)\nabla\hat{u}(t)-\frac{1}{\lambda}\tilde{p}(t)\nabla\tilde{u}(t)\Bigg), \\ q^{n+1}(t)&=q^n(t)+\Delta t\nabla\cdot b^n(t). \end{aligned} \tag{12}$$

In [27] is shown that this explicit (forward Euler) time marching scheme is conditionally stable, i.e. the time step Δt should be selected in a manner which gives sufficient decrease in the functional. However, the forward scheme has rather undesirable asymptotic convergence properties which can make it inefficient. To get ride of that Vogel and Oman introduced the lagged diffusivity fixed point iteration, denoted by FP-iteration, in [27]. The FP-iteration linearizes the non-linear diffusion part in (12) at iteration $n+1$, i.e. we apply the diffusion operator

$$DF(b^n)v=\nabla\cdot\left(\frac{\nabla v}{|\nabla b^n|_\varepsilon}\right)$$

at the active iteration $n+1$. Hence, we can formulate it into an implicit scheme

$$\left(1-\Delta t DF(b^n)\right)b^{n+1}=z,$$

where z denotes the rest terms not involving b^{n+1}. In [28] it was shown that this algorithm is robust and globally linearly convergent. The details of underlying scheme according to v read as follows (using the notation $b=(v,w)$):

$$\begin{aligned} \partial_x\left(\frac{v_x^{n+1}}{|\nabla b^n|_\varepsilon}\right)&=\partial_x\left(|\nabla b^n|_\varepsilon^{-1}\right)v_x^{n+1}+\frac{v_{xx}^{n+1}}{|\nabla b^n|_\varepsilon} \\ &=-|\nabla b^n|_\varepsilon^{-3}\Big(v_x^n v_{xx}^n+v_y^n v_{xy}^n \\ &\qquad +w_x^n w_{xx}^n+w_y^n w_{xy}^n\Big)v_x^{n+1}+\frac{v_{xx}^{n+1}}{|\nabla b^n|_\varepsilon}, \end{aligned}$$

$$\begin{aligned} \partial_y\left(\frac{v_y^{n+1}}{|\nabla b^n|_\varepsilon}\right)&=\partial_y\left(|\nabla b^n|_\varepsilon^{-1}\right)v_y^{n+1}+\frac{v_{yy}^{n+1}}{|\nabla b^n|_\varepsilon} \\ &=-|\nabla b^n|_\varepsilon^{-3}\Big(v_x^n v_{xy}^n+v_y^n v_{yy}^n \\ &\qquad +w_x^n w_{xy}^n+w_y^n w_{yy}^n\Big)v_y^{n+1}+\frac{v_{yy}^{n+1}}{|\nabla b^n|_\varepsilon}. \end{aligned}$$

Altogether the discretization of (12) with respect to v yields

$$\begin{aligned} &v^{n+1}+\Delta t\,|\nabla b^n|_\varepsilon^{-3}\left(v_x^n v_{xx}^n+v_y^n v_{xy}^n+w_x^n w_{xx}^n+w_y^n w_{xy}^n\right)v_x^{n+1} \\ &\quad -\Delta t\frac{v_{xx}^{n+1}}{|\nabla b^n|_\varepsilon}+\Delta t\,|\nabla b^n|_\varepsilon^{-3}\Big(v_x^n v_{xy}^n+v_y^n v_{yy}^n+w_x^n w_{xy}^n \\ &\quad +w_y^n w_{yy}^n\Big)v_y^{n+1}-\Delta t\frac{v_{yy}^{n+1}}{|\nabla b^n|_\varepsilon} \\ &\quad =v^n+\frac{\Delta t}{\lambda}q_x^n-\frac{\Delta t}{\lambda}\left(\hat{p}\hat{u}_x+\tilde{p}\tilde{u}_x\right). \end{aligned}$$

Similarly, solving (11) we also use a time-marching scheme and apply the FP-iteration.

A. Segregation Loop

As explained in Section III we apply a modified segregation loop to solve the equation system (8)–(11). We suppose $n=1,\cdots,N_{\text{loop}}$ and N_{loop} is the iteration number. Given $u_0,u_T,b^{n-1}(t),\phi^{n-1},\lambda,\mu,\nu$. The iteration process at iteration n proceeds as follows:

1) Compute $\hat{u}^{n-1}(t),\nabla\hat{u}^{n-1}(t)$ and $\hat{u}^{n-1}(T)$ using u_0 and $b^{n-1}(t)$.
2) Compute $\hat{p}^{n-1}(t)$ using $\hat{u}^{n-1}(T),u_T$ and $H_s(\phi^{n-1})$.
3) Compute $\tilde{u}^{n-1}(t),\nabla\tilde{u}^{n-1}(t)$ and $\tilde{u}^{n-1}(0)$ using u_T and $b^{n-1}(t)$.
4) Compute $\tilde{p}^{n-1}(t)$ using $\tilde{u}^{n-1}(0),u_0$ and $H_s(\phi^{n-1})$.
5) Compute the solution of the TV$_\varepsilon$-Stokes equations with right-hand side $\hat{p}^{n-1}(t)\nabla\hat{u}^{n-1}(t)+\tilde{p}^{n-1}(t)\nabla\tilde{u}^{n-1}(t)$. Then, denote it by $\delta b^{n-1}(t)$.
6) Compute solution ϕ^n of (11) using $\hat{u}(T),u_T,\tilde{u}(0),u_0$ and ϕ^{n-1} as the initial value of the time-marching scheme.
7) Update $b^n(t)=b^{n-1}(t)+\delta b^{n-1}(t)$.

Similar to the segregation loop in Section III, this segregation loop does not solve the original problem, but actually approximates a solution of the necessary conditions of another minimizing problem, namely: Minimize

$$\frac{1}{2}\left\|\hat{u}(T)-u_T\right\|_{L^2(\omega)}^2+\frac{1}{2}\left\|\tilde{u}(0)-u_0\right\|_{L^2(\Omega\setminus\overline{\omega})}^2$$

subject to

$$\begin{cases} \hat{u}_t+b\cdot\nabla\hat{u}=0 \ \text{ in }]0,T]\times\Omega \ \text{ with } \hat{u}(0)=u_0 \ \text{ in } \Omega, \\ \tilde{u}_t+b\cdot\nabla\tilde{u}=0 \ \text{ in } [0,T[\times\Omega \ \text{ with } \tilde{u}(T)=u_T \ \text{ in } \Omega \\ \operatorname{div} b=0 \ \text{ in } [0,T]\times\Omega \ \text{ with } b=0 \text{ on } \partial\Omega. \end{cases}$$

Again, we may see the segregation loop as a kind of a Landweber method for minimizing $\frac{1}{2}\|\hat{u}(T) - u_T\|^2_{L^2(\omega)} + \frac{1}{2}\|\tilde{u}(0) - u_0\|^2_{L^2(\Omega\setminus\overline{\omega})}$ which is inspired by a special Tikhonov-functional.

B. Implementation

In optical flow estimation it is common to use the hierarchical processing (cf. [29], [30]) to handle large displacements, and we apply this technique to get a start value b^0 for the optimality system. We execute the following procedure

1) Down-sample the images into level l.
2) Carry out the segregation loop in level l out and get b^l.
3) Up-sample the optical flow into level $l-1$ and get b^{l-1}

The estimated optical flow b^{l-1} is a start value of the hierarchical method in level $l-1$ and we repeat it until level 0. In the coarsest level we assume the start value to be zero.

The essential parameters of the quality of image sequence interpolation are the regularization parameters λ, μ, ν. The parameter λ depends strongly on the intensities of the optical flow (velocities). For larger velocities we have to penalize it with larger λ. In the praxis, if the velocities are smaller than 25 pixels between two image then we can set $\lambda \in [10^{4.4}, 10^5]$. The parameters μ, ν, which involves the segmentation we set both equal to 1. Regarding the time step in the time-marching scheme of the parabolic equations for optical flow and segmentation we set $\Delta t = 10^3$, since the implicit method is stable with arbitrary time step. Then in few steps we can achieve the convergence. The smoothing parameter ε we set equal to 1 and s equal to 10^{-2}.

All datasets we considering are 8 bit RGB color images. Dealing with the RGB color images we convert them into 8 bit grayscale first, calculate the optical flow and active contours, and at the end warp every color channel with that flow field.

C. Experiments and Evaluation

To visualize the flow field both in angles and intensities we utilize the color coding map in Fig. 1 (cf. [17]). The direction of the flow is coded by hue and the intensity is coded by saturation, i.e. the brighter the color the larger the velocity.

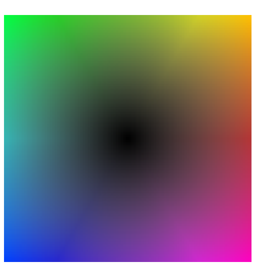

Fig. 1. Color coding map of optical flow.

We compare the new introduced method, denoted by the TV$_\varepsilon$-segment method, with the smooth method introduced in [18]. To illustrate the ability to handle disclusions and occlusions we apply them on the dataset MiniCooper. Firstly, Fig. 3 shows that the TV$_\varepsilon$-segment method preserves the flow edges better than the smooth method. Consequently, the interpolation by the TV$_\varepsilon$-segment keeps the boundary of objects (shapes) better than the smooth method. Additionally, the associated active contours for segmentation are also shown in Fig. 3. In Fig. 4 we present the interpolated image of dataset in Fig. 2 at time $T/2$ by the smooth method and TV$_\varepsilon$-segment method. The associated zoomed-in sub-images in Fig. 5 show that the TV$_\varepsilon$-segment method interpolated the disclosed regions (the upper part of head and the rear of the car) better than the smooth method. Comparing the zoomed-in sub-contours we can easily establish that the segmentation process has successfully identified the "covered" regions (the bottom part of the head) and the "disclosed' 'regions (the top part of the head and the rear of the car).

To evaluate our image sequence interpolation method we performed an experiment based on human visual perception. We choose 4 artificial datasets Face, Earth, Bunny and Dragon from ftp://graphics.tu-bs.de/pub/public/people/lipski/stimuli/ (see Fig. 6). The dataset Face is composed of 60 images and other each dataset is composed of around 120 images. We compare our methods with other 7 existing methods from [15] for which interpolation results have been available, and we designed the experiment in the following way: Among every four images two middle images are taken out and using the first and last one the missing images will be interpolated (i.e. we performed a subsampling with respect to time by the factor of 3). Now, each participant in our experiment is shown two interpolation results side by side and is asked which one looks better. For each of the scenes we compare all 7 interpolation methods and the ground-truth against each other (only comparing method A and method B, excluding self-comparison and the reverse comparison method B to method A). This yields a total of $4 \cdot (8 \cdot 7/2) = 112$ trials per participant. We denote N the number of participants and in each trial the perceptually better image gets 1 point. After all trials we divide the score of every algorithm of each dataset by $7N$ and all datasets by $35N$ to get the normalized score for every dataset and all datasets. The range of the score is in $[0, 1]$ and a higher score stands for better human visual perception.

	Face	Earth	Bunny	Dragon	**average**
original	0.90	0.86	0.88	0.96	**0.90**
blend	0.24	0.14	0.32	0.26	**0.24**
opticalflow	0.01	0.02	0.02	0.02	**0.02**
nofeathering	0.49	0.50	0.35	0.50	**0.46**
nooptim	0.26	0.32	0.39	0.21	**0.29**
full	0.50	0.53	0.42	0.51	**0.49**
multiscale	0.82	0.82	0.84	0.82	**0.82**
TV$_\varepsilon$-segment	0.77	0.82	0.78	0.73	**0.78**

TABLE I
THE FIRST FOUR COLUMNS GIVE THE NORMALIZED SCORES OF THE ALGORITHMS FROM [15] AND TV$_\varepsilon$-SEGMENT APPLIED ON EVERY DATASET. THE NEXT COLUMN GIVES THEIR AVERAGE SCORES OF THESE DATASETS.

In total 17 participants took part in this experiment, and in Table I we can observe that the so called "multi-scale" and TV$_\varepsilon$-segment methods visual perceptually perform better than the other methods.

In Table II we also evaluate the RMSE [17], that is the root-mean-square error between the ground-truth image u_{GT} and the interpolated image u:

$$RSME = \left(\frac{1}{MN} \sum_{i=1}^{N} \sum_{j=1}^{M} (u(x_i, y_j) - u_{\mathrm{GT}}(x_i, y_j))^2 \right)^{\frac{1}{2}},$$

where $M \times N$ is the image size. Observe that the TV_ε-segment method does not outperform the "nooptim" and "full" methods with respect to the RSME, which is in contrast to the results from the visual perception. The RMSE does not reveal human visual perception due to two reasons. Firstly, the human eyes are sensitive for the shocks which are the common drawbacks of the opticalflow, nofeathering, full methods (see e.g. Fig. 10), and also sensitive for the ghosting effects, which are characterized by the blend method (cf. Figs. 8 (a) and 10 (a)). Secondly, there are indeed many ways to interpolate, but this does not mean that all results are possible ground-truth data. In addition to the experimental results we present examples of interpolated images in Figs. 7, 8, 9 and 10. Again, our method correctly identifies the regions (the white in the associated contours images) in which occlusions occur (in dataset Earth/Bunny on the left/right hand side of the objects where parts of the objects "disappear", respectively).

	Face	Earth	Bunny	Dragon	**average**	Plant
blend	3.73	4.18	2.41	3.49	**3.45**	8.09
opticalflow	3.11	4.25	2.36	3.38	**3.28**	10.26
nofeathering	1.72	1.52	1.40	2.02	**1.67**	6.79
nooptim	2.29	2.15	1.95	2.58	**2.24**	7.34
full	1.72	1.52	1.40	2.02	**1.67**	6.80
multiscale	1.31	0.75	1.16	1.97	**1.31**	6.73
TV_ε-segment	2.08	1.91	1.65	2.40	**1.99**	6.69

TABLE II
THE FIRST FOUR COLUMNS GIVE THE RMSE OF THE ALGORITHMS FROM [15] AND TV_ε-SEGMENT APPLIED ON EVERY DATASET. THE FIFTH COLUMN GIVES THE AVERAGE RMSE OF EVERY ALGORITHM APPLIED TO THESE DATASETS. THE LAST COLUMN GIVES THE RMSE OF EVERY ALGORITHM APPLIED ON THE REAL DATASET PLANT.

In the last example we consider the real video sequence "Plant"[2] (Fig. 11) consisting of 124 images. Again, we performed a temporal downsampling by a factor of three and interpolated the missing frames. Comparing our interpolated images to the ground-truth images (difference coded in the red color) in Figure 11 and the RMSE in Table II, we can conclude that our interpolation method works also well with real video sequences. Although the difference of the interpolated frames to the ground truth is quite large, the interpolated movie looks natural.

All these routines in the segregation loop were implemented in Matlab on a Windows 7 with Intel Core i7 Q720 CPU. The computational time is strongly related to image size and iteration number N_{loop}, e.g. using a 641×480 image in finest resolution level 0 applying 5 iterations the elapsed time is 780 seconds and in one level coarser resolution with the same iteration number the elapsed time is always approximately 4 times less. In all experiments we used the iteration numbers $[20, 20, 20, 20, 5]$ from coarsest level to finest level in the hierarchical processing.

[2] Also available at ftp://graphics.tu-bs.de/pub/public/people/lipski/stimuli/.

VI. Conclusion and Outlook

The approach to image sequence interpolation based on the optical flow in the framework of optimal control avoids shocks and ghosting effects. The improvement by TV_ε-flow and segmentation showed that it is able to produce more natural interpolation for human visual perception. However, as already explained in [18], this method has a limited application if the illumination of object varies in time, since we only consider the transport equation with right-hand side 0. This means that the external illumination variation, e.g. light or flash, does not come to consideration.

In further work it might be interesting to introduce another control f in the right-hand side of the transport equation to simulate the external illumination variation. However, since the movement of an object can also be generated as a drastical change "illumination", it might be difficult to obtain meaningful results for both b and f.

Acknowledgment

The authors would like to thank all the participants who joined the visual perceptual experiment.

References

[1] J. Watkinson, *The MPEG Handbook*, 2nd ed. Focal Press, 2004.
[2] D. Rueckert, L. I. Sonoda, C. Hayes, D. L. G. Hill, M. O. Leach, and D. J. Hawkes, "Nonrigid registration using free-form deformations: Application to breast MR images," *IEEE Transactions on Medical Imaging*, vol. 18, pp. 712–721, 1999.
[3] J. M. Fitzpatrick and M. Sonka, *"Handbook of Medical Imaging, Volume 2. Medical Image Processing and Analysis"*, 1st ed. SPIE, 2000.
[4] B. K. P. Horn and B. G. Schunck, "Determining optical flow," *Artificial Intelligence*, vol. 17, pp. 185–203, 1981.
[5] G. Aubert and P. Kornprobst, "A mathematical study of the relaxed optical flow problem in the space $BV(\Omega)^*$," *SIAM Journal on Mathematical Analysis*, vol. 30, pp. 1282–1308, 1999.
[6] A. Bruhn, J. Weickert, and C. Schnörr, "Lucas/Kanade meets Horn/Schunck: Combining local and global optic flow methods," *International Journal of Computer Vision*, vol. 61, pp. 211–231, 2005.
[7] H. H. Nagel, "Constraints for the estimation of displacement vector fields from image sequences," in *In International Joint Conference on Artificial Intelligence*, 1983, pp. 945–951.
[8] W. Enkelmann, "Investigation of multigrid algorithms for the estimation of optical flow fields in image sequences," *Computer Vision, Graphics, and Image Processing*, vol. 43, pp. 150–177, 1988.
[9] A. Wedel, T. Pock, C. Zach, H. Bischof, and D. Cremers, "An Improved Algorithm for TV-L1 Optical Flow," in *Statistical and Geometrical Approaches to Visual Motion Analysis*, 2009.
[10] S. L. Keeling and W. Ring, "Medical image registration and interpolation by optical flow with maximal rigidity." *Journal of Mathematical Imaging and Vision*, vol. 23, no. 1, pp. 47–65, 2005.
[11] E. Mémin and P. Pérez, "Dense estimation and object-based segmentation of the optical flow with robust techniques," *IEEE Trans. Image Processing*, vol. 7, no. 5, pp. 703–719, 1998.
[12] W. Hinterberger and O. Scherzer, "Models for image interpolation based on the optical flow," *Computing*, vol. 66, pp. 231–247, 2001.
[13] A. Borzí, K. Ito, and K. Kunisch, "Optimal control formulation for determining optical flow," *SIAM Journal of Scientific Computing*, vol. 24, pp. 818–847, 2002.
[14] D. Mahajan, F. Huang, W. Matusik, R. Ramamoorthi, and P. Belhumeur, "Moving gradients: a path-based method for plausible image interpolation." *ACM Transactions on Graphics*, vol. 28, no. 3, 2009.

[15] T. Stich, C. Linz, C. Wallraven, D. Cunningham, and M. Magnor, “Perception-motivated interpolation of image sequences,” in *Proc. ACM Symposium on Applied Perception in Graphics and Visualization (APGV)*, 2008, pp. 97–106.
[16] ——, “Time and View Interpolation in Image Space,” *Computer Graphics Forum (Proc. Pacific Graphics’08)*, vol. 27, no. 7, pp. 1781–1787, 2008.
[17] S. Baker, D. Scharstein, J. P. Lewis, S. Roth, M. J. Black, and R. Szeliski, “A database and evaluation methodology for optical flow,” *International Journal of Computer Vision*, vol. 92, pp. 1–31, 2011.
[18] K. Chen and D. Lorenz, “Image sequence interpolation using optimal control,” *Journal of Mathematical Imaging and Vision*, 2011.
[19] T. F. Chan and L. A. Vese, “Active contours without edges,” *IEEE Transactions on Image Processing*, vol. 10, no. 2, 2001.
[20] V. Caselles, F. Catté, T. Coll, and F. Dibos, “A geometric model for active contours in image processing,” *Numerische Mathematik*, vol. 66, pp. 1–31, 1993.
[21] M. Kass, A. Witkin, and D. Terzopoulos, “Snakes: Active contour models,” *International Journal of Computer Visiony*, vol. 1, no. 4, pp. 321–331, 1988.
[22] D. Mumford and J. Shah, “Optimal approximations by piecewise smooth functions and associated variational problems,” *Communications on Pure and Applied Mathematics*, vol. 42, no. 5, pp. 577–685, 1989.
[23] C. Hirsch, *Numerical Computation of Internal & External Flows*. Elsevier, 2007.
[24] K. F. Riley, M. P. Hobson, and S. J. Bence, *Mathematical Methods for Physics and Engineering*. Cambridge University Press, 2006.
[25] X. C. Tai, S. Osher, and I. Holm, “Image inpainting using a TV-Stokes equation,” in *Image Processing based on partial differential equations*. Heidelberg: Springer, 2006.
[26] W. H. Press, S. A. Teukolsky, W. T. Vetterling, and B. P. Flannery, *Numerical Recipes 3rd Edition: The Art of Scientific Computing*, 3rd ed. Cambridge University Press, 2007.
[27] C. R. Vogel and M. E. Oman, “Iterative methods for total variation denoising,” *SIAM Journal on Scientific Computing*, vol. 17, pp. 227–238, 1996.
[28] T. F. Chan and P. Mulet, “On the convergence of the lagged diffusivity fixed point method in total variation image restoration,” *SIAM Journal on Numerical Analysis*, vol. 36, no. 2, pp. 354–367, 1999.
[29] J. L. Barron and M. Khurana, “Determining optical flow for large motions using parametric models in a hierarchical framework,” in *In Vision Interface*, 1994, pp. 47–56.
[30] T. Brox, A. Bruhn, N. Papenberg, and J. Weickert, “High accuracy optical flow estimation based on a theory for warping,” in *Computer Vision - ECCV 2004*. Springer, 2004, pp. 25–36.

Kanglin Chen received the Diplom degree from University of Bremen, Germany in 2008. Since 2008 he attended the Ph.D. program SCiE (Scientific Computing in Engineering) at University of Bremen and graduated in September 2011.

Dirk A. Lorenz received his Diplom degree and his Ph.D. in Mathematics from University of Bremen, Germany in 2002 and 2005, respectively. Since 2009 he is “Juniorprofessor” (equiv. to assistant professor) for applied analysis at TU Braunschweig, Germany. His research interests include mathematical image processing, inverse problems and optimization.

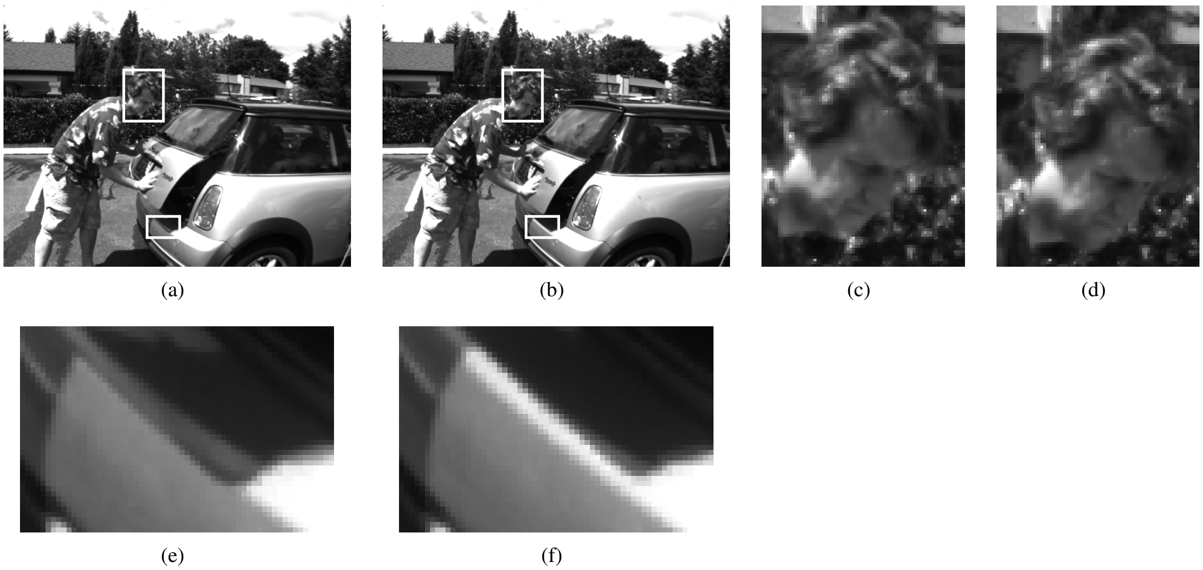

Fig. 2. (a) Frame 10. (b) Frame 11. (c) The zoomed-in region of the head area in (a). (d) The zoomed-in region of the head area in (b). (e) The zoomed-in region of the rear of the car in (a). (f) The zoomed-in region of the rear of the car in (b).

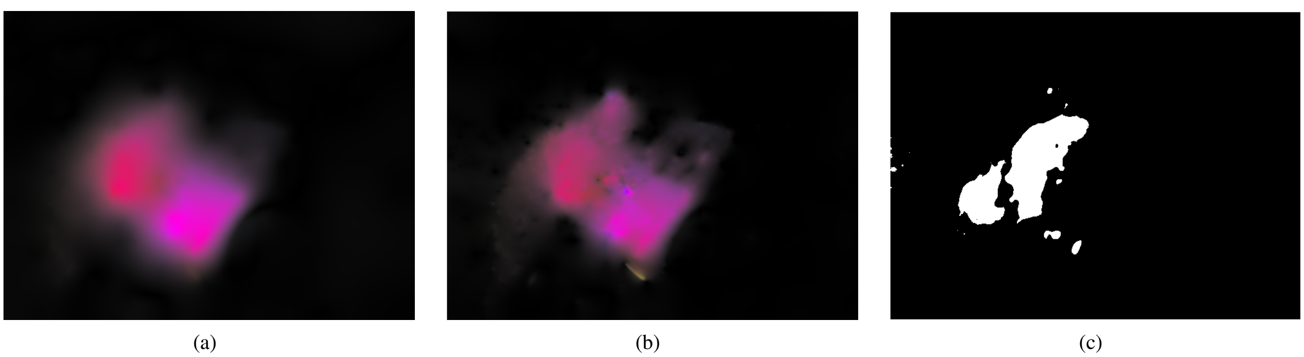

Fig. 3. Experiment on frame 10 and 11 of Fig. 2. (a) The optical flow calculated by the smooth method. (b) The optical flow calculated by the TV$_\varepsilon$-segment method. (c) The active contours calculated by the TV$_\varepsilon$-segment method. The black refers to the backward interpolation region and the white refers to the forward interpolation region.

Fig. 4. Experiment on frame 10 and 11 of Fig. 2. (a) The interpolated frame by the smooth method at time $T/2$. (b) The interpolated frame by the TV$_\varepsilon$-segment method at time $T/2$.

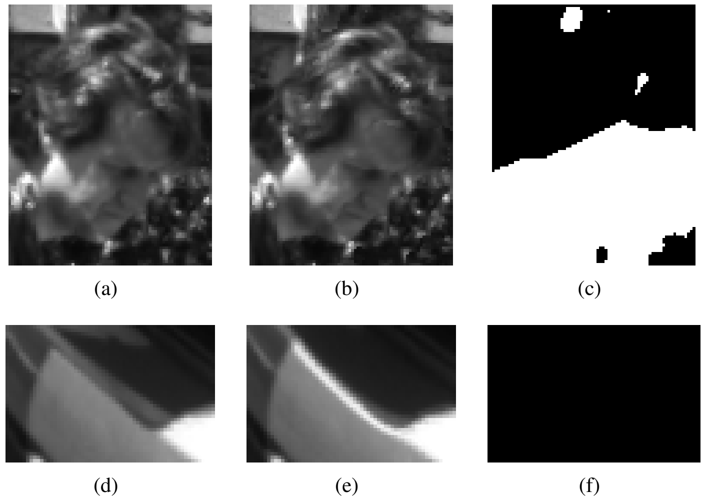

Fig. 5. (a) The zoomed-in region of the head area in (a) of Fig. 4. (b) The zoomed-in region of the head area in (b) of Fig. 4. (c) The zoomed-in region of the contours of the head area generated by the TV_ε-segment method. (d) The zoomed-in region of the rear of the car in (a) of Fig. 4. (e) The zoomed-in region of the rear area of the car in (b) of Fig. 4. (f) The zoomed-in region of the contours of the rear of the car generated by the TV_ε-segment method.

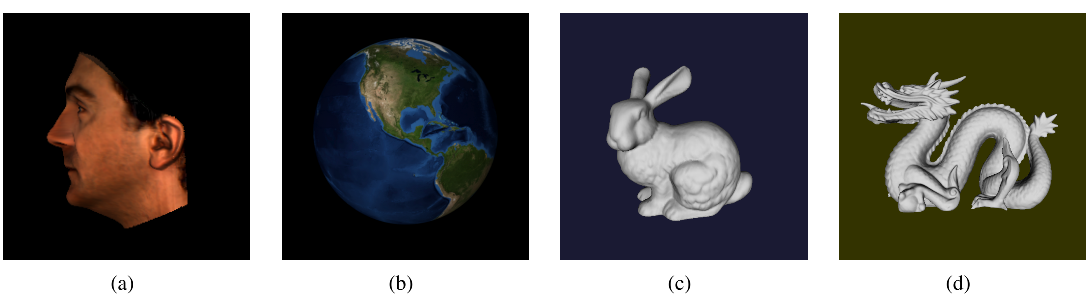

Fig. 6. Datasets of Stich. (a) Face. (b) Earth. (c) Bunny. (d) Dragon.

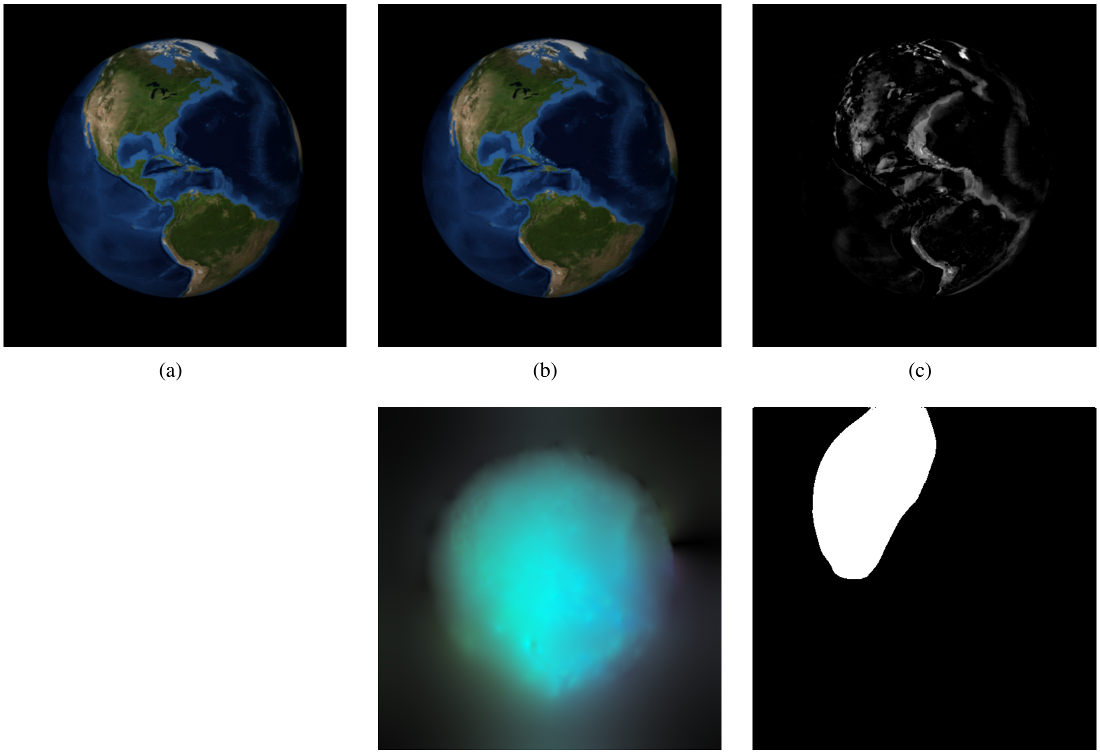

(a) (b) (c)

(d) (e)

Fig. 7. (a) Frame 9 of Earth. (b) Frame 12 of Earth. (c) The absolute difference of (a) and (b). (d) The optical flow calculated by the TV_ε-segment method. (e) The active contours of segmentation calculated by the TV_ε-segment method.

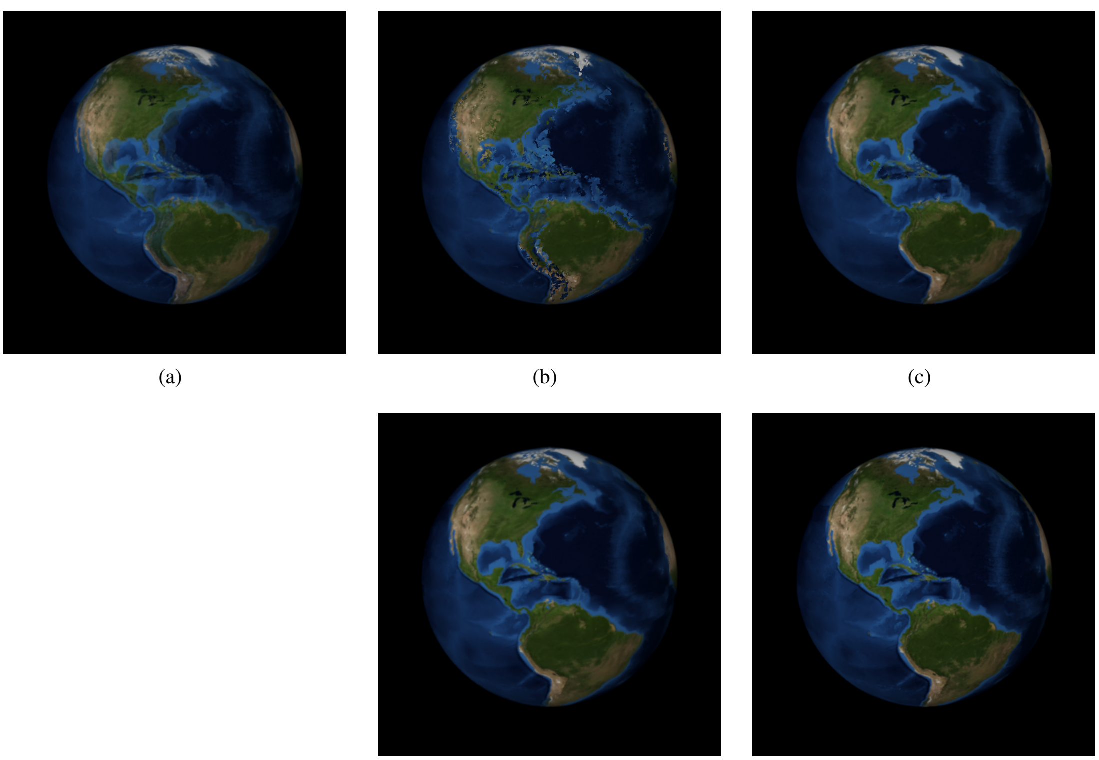

(a) (b) (c)

(d) (e)

Fig. 8. Frame 11 calculated by (a) the blend method (b) the opticalflow method (c) the full method (d) the multiscale method (e) the TV_ε-segment method.

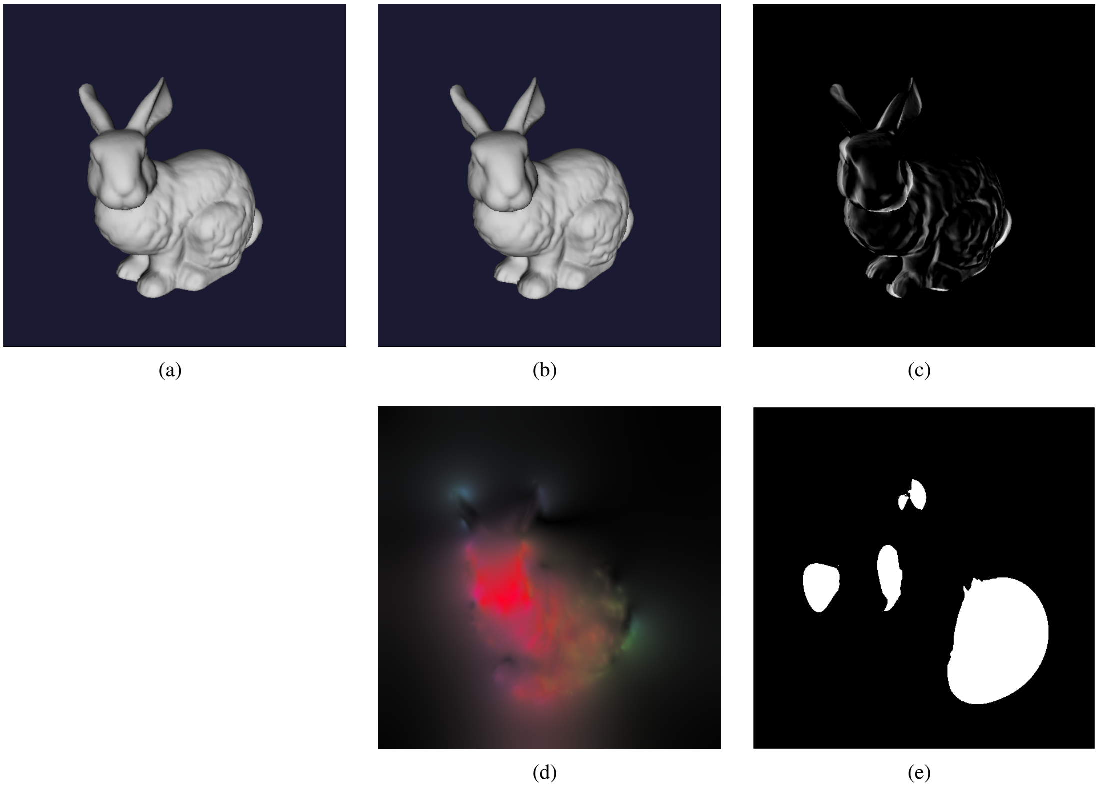

Fig. 9. (a) Frame 15 of Bunny. (b) Frame 18 of Bunny. (c) The absolute difference of (a) and (b). (d) The optical flow calculated by the TV$_\varepsilon$-segment method. (e) The active contours of segmentation calculated by the TV$_\varepsilon$-segment method.

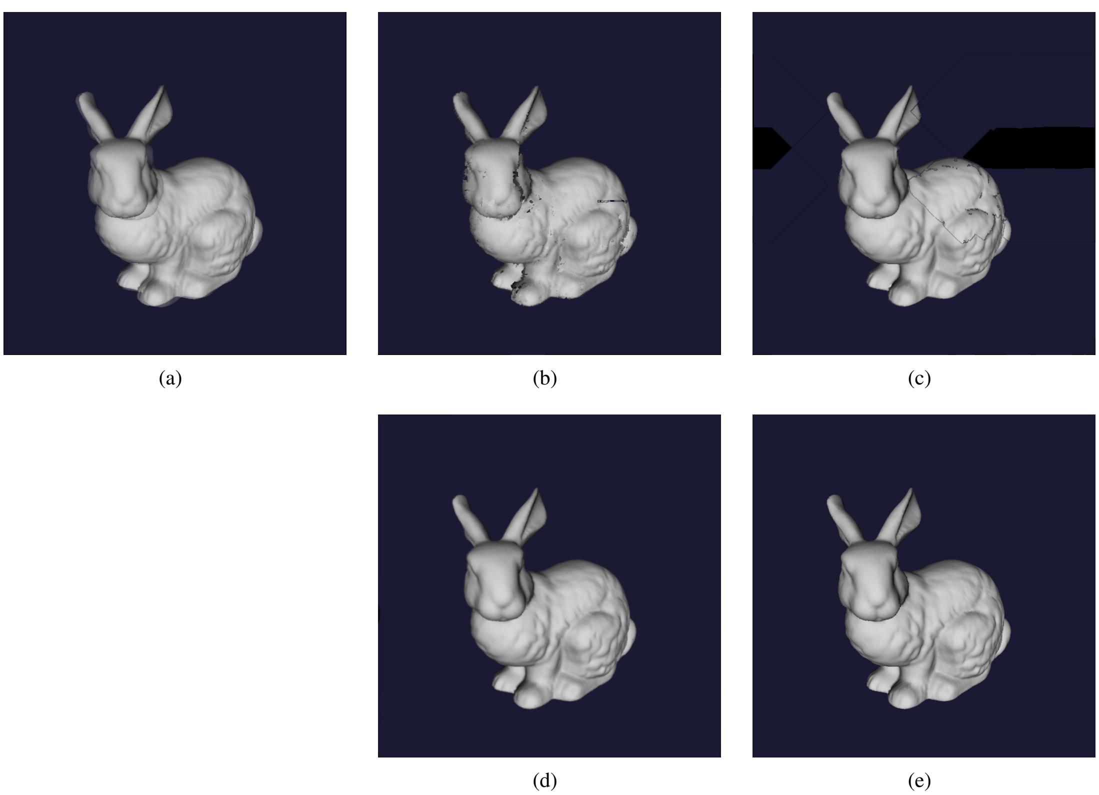

Fig. 10. Frame 16 calculated by (a) the blend method (b) the opticalflow method (c) the full method (d) the multiscale method (e) the TV$_\varepsilon$-segment method.

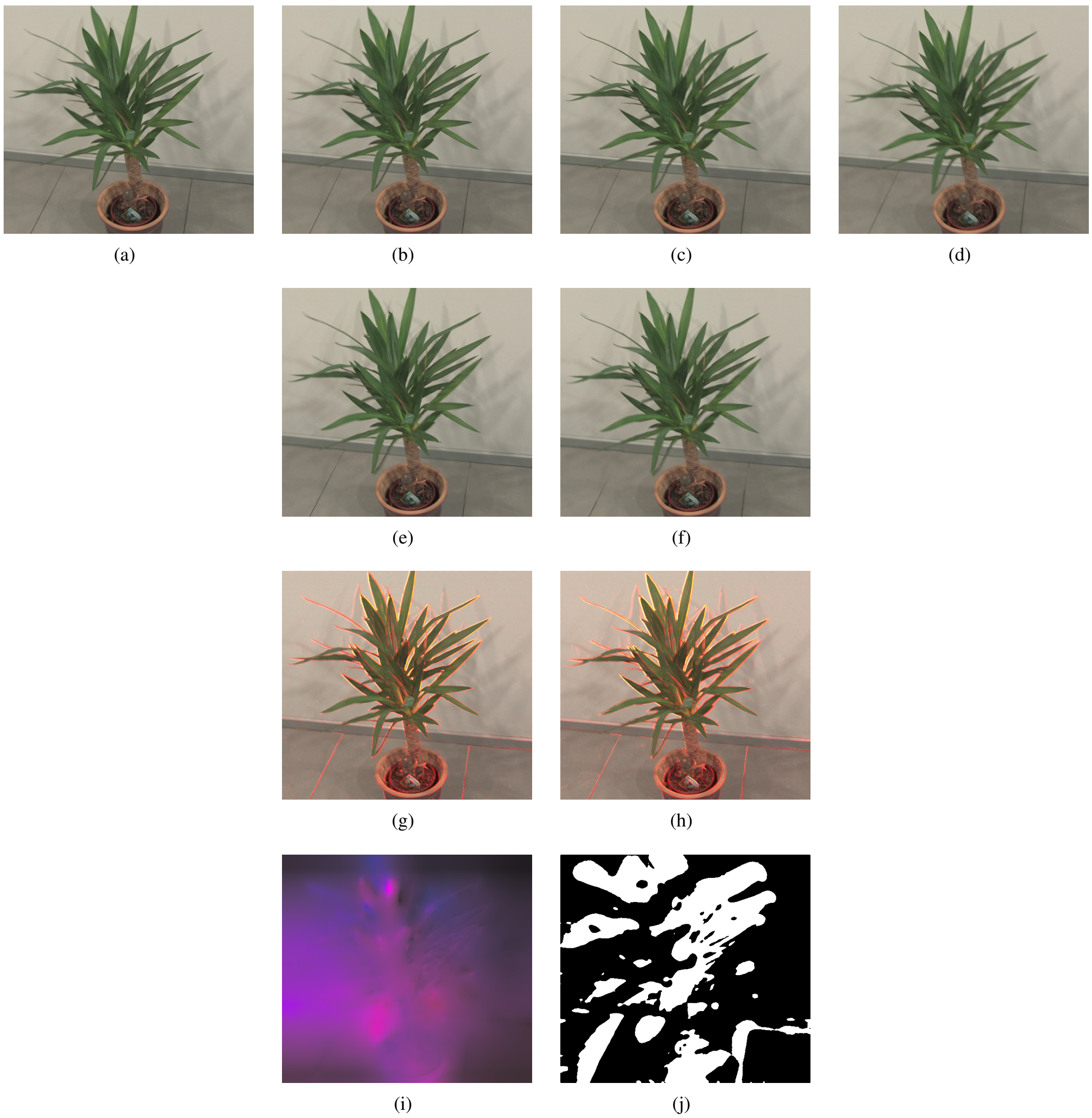

Fig. 11. (a) Frame 54. (b) Ground truth frame 55. (c) Ground truth frame 56 (d) Frame 57. (e) Interpolated frame 55 calculated by the TV_ε-segment method. (f) Interpolated frame 56 calculated by the TV_ε-segment method. (g) Frame 55 calculated by the TV_ε-segment method plus the colored difference compared to the ground-truth. (h) Frame 56 calculated by the TV_ε-segment method plus the colored difference compared to the ground-truth. (i) The optical flow calculated by the TV_ε-segment method. (j) The active contours calculated by the TV_ε-segment method.